Sidelobe suppression and axial resolution enhancement in 4pi microscopy with higher-order radially polarized Laguerre–Gaussian beams using subtractive imaging

Zhiyuan Gu (顾志远), Xianghui Wang (王湘晖)*, Jianxin Wang (王建鑫), Fei Fan (范 飞), and Shengjiang Chang (常胜江)

Institute of Modern Optics, Tianjin Key Laboratory of Optoelectronic Sensor and Sensing Network Technology, Nankai University, Tianjin 300350, China

**Corresponding author: wangxianghui@nankai.edu.cn*

Received June 17, 2019; accepted August 22, 2019; posted online December 2, 2019

Subtractive imaging is used to suppress the axial sidelobes and improve the axial resolution of 4pi microscopy with a higher-order radially polarized (RP) Laguerre–Gaussian (LG) beam. A solid-shaped point spread function (PSF) and a doughnut-shaped PSF with a dark spot along the optical axis are generated by tightly focusing a higher-order RP-LG beam and a modulated circularly polarized beam, respectively. By subtracting the two images obtained with those two different PSFs, the axial sidelobes of the subtracted PSF are reduced from 37% to about 10% of the main lobe, and the axial resolution is increased from 0.21λ to 0.15λ.

OCIS codes: 110.0180, 100.6640, 170.0180, 180.6900.
doi: 10.3788/COL201917.121103.

How to improve the spatial resolution of optical microscopy always has great significance and attracts a lot of interest[1,2]. Usually, the resolution is directly related to the focal spot size of the optical imaging system. The narrower the focal spot, the higher the resolution. It has been theoretically and experimentally demonstrated that when a radially polarized (RP) beam is tightly focused by a high numerical aperture (NA) objective, a strong longitudinal electric field is produced, and then a sharper focal spot in comparison to linearly polarized ones is formed[3,4], which has widespread applications in many fields, such as optical trapping[5], super-resolution microscopy[6], and material processing[7]. This RP beam is commonly referred to as a fundamental RP mode. Higher-order RP Laguerre–Gaussian (LG) beams represented by RP-$LG_{p,1}$ can also be experimentally generated in a laser cavity[8] or by using a spatial light modulator to modulate the phase distribution of the incident beam[9]. Here, the subscript p denotes the radial mode number, which indicates that a higher-order RP-LG beam has a multiring-shaped intensity pattern with $p+1$ concentric rings[10]. There is a π phase shift between the two adjacent rings. In the case of high-NA focusing, those higher-order RP-LG beams have much better lateral resolution compared with the fundamental RP mode as the radial mode number p increases[11,12]. It is attributed to the destructive interference near the focal point induced by the phase shifts of the multiring beam pattern. However, it also should be noted that the lateral resolution is enhanced at the cost of the axial extension[13]. In other words, the focal field distribution is elongated along the optical axis with the increasing radial mode number p, which indicates the decrease of the axial resolution and compromises the sectioning ability of the optical imaging system[11]. A 4pi focusing system has been proposed to improve the axial resolution[14]. In a 4pi configuration, two counter-propagating beams are focused by two opposing high-NA objectives, and there is a common geometrical focus point between the two objectives[15,16]. Due to the interference of those two coherent beams, the central lobe of the intensity point spread function (PSF) in the axial direction could be almost several times narrower compared with the results in the case of the single-lens focusing configuration[17,18]. Sadly, one problem of this strategy is the generation of stronger axial sidelobes[14], which is much likely to result in ambiguity in the image and limited practicability of the imaging system. Furthermore, the case becomes more severe as the radial mode number p increases.

In order to eliminate the undesirable effect on the imaging quality induced by stronger axial sidelobes, several methods have been proposed to overcome this problem. For example, two-photon excitation[18] and deconvolution techniques[19] have been used to reduce the height of the axial sidelobes in 4pi microscopy. The disadvantages of two-photon excitation are photodamage of the sample induced by intense illumination and limitation of appropriate fluorophores. Compared with optical solutions, data deconvolution techniques are much more complex. Under linearly polarized illumination, the effect of axial sidelobes can be suppressed by inserting amplitude-type pupil filters[20] or Toraldo rings[21] in two arms of the illumination path. However, for the case of higher-order RP-LG beams, the intrinsic multiring beam pattern will be disturbed by those filters or rings.

Subtractive imaging has been reported to increase the resolution of confocal laser-scanning microscopy. It acquires a higher-resolution image by subtracting two images obtained under different conditions[22,23]. The performance

of an imaging system can be enhanced just by a mathematical subtraction to a certain extent, and there is no need to greatly update the hardware of the existing setups. Therefore, subtraction imaging is much simpler and more effective. Recently, the subtractive imaging technique has been proposed to enhance the axial resolution of line-scanning temporal focusing microscopy[24] or to suppress the influence of the axial sidelobes in light-sheet fluorescence microscopy[25,26]. By subtracting two images acquired with an extended solid Bessel beam and a ring-like Bessel beam, the sidelobe suppression is realized, and the sectioning ability is also enhanced[25]. For line-scanning temporal focusing microscopy, the axial resolution is increased, and background noise is rejected by simply subtracting an aberrated image from an unaberrated image[24]. The improvement of the lateral resolution of confocal microscopy with higher-order LG beams has been demonstrated by image subtraction between images obtained by RP and azimuthally polarized (AP) LG mode beams[9]. However, to the best of our knowledge, little attention has been paid to using subtractive imaging to reduce the undesirable effect of the axial sidelobes and enhance the axial resolution in 4pi microscopy with higher-order RP-LG beams.

In this Letter, RP-$LG_{1,1}$ beams and modulated circularly polarized beams are tightly focused in a 4pi imaging system to produce a solid-shaped PSF and a doughnut-shaped PSF, respectively. The doughnut-shaped PSF has a dark spot in the longitudinal direction. By subtracting an image obtained with the doughnut-shaped PSF from an image obtained with the solid-shaped PSF, the sidelobe height of the subtracted axial PSF can be reduced from 37% of the main lobe to about 10%. In addition, the axial resolution of the 4pi imaging system is enhanced from 0.21λ to 0.15λ, and the lateral resolution nearly remains unchanged. Furthermore, the optical transfer function (OTF) of the system is analyzed. The image reconstruction of a three-dimensional (3D) sample with a 3-by-3-by-3 point array is presented to demonstrate the improvement of the sectioning ability and image quality.

Figure 1 shows the typical geometry of a 4pi focusing system with two opposing high-NA objectives. For simplification, the focusing objectives are assumed to be infinity-corrected. The two incident wave fronts coherently interfere in the focal region, and then the total aperture

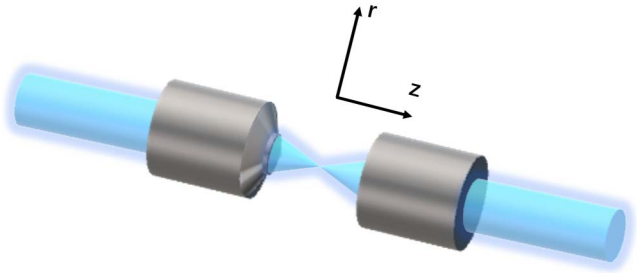

Fig. 1. Diagram of 4pi focusing configuration. The lateral and axial directions are denoted by the r axis and z axis, respectively.

along the axial direction is doubled[15]. Usually, there are three types of 4pi microscopy. For a type-C 4pi configuration, the two focusing objectives are coherently illuminated by two counter-propagating beams and are also used to collect the fluorescent signal emitted from the sample. Therefore, the PSF of the type-C 4pi microscopy is given by[17]

$$\mathrm{PSF}_{\mathrm{4pi\text{-}c}} = \mathrm{PSF}_{\mathrm{ill}} \cdot \mathrm{PSF}_{\mathrm{det}}, \tag{1}$$

where $\mathrm{PSF}_{\mathrm{ill}}$ and $\mathrm{PSF}_{\mathrm{det}}$ are the illumination and detection PSFs, respectively. $\mathrm{PSF}_{\mathrm{ill}}$ and $\mathrm{PSF}_{\mathrm{det}}$ can be expressed as

$$\mathrm{PSF}_{\mathrm{ill}}(r,z) = \left|\boldsymbol{E}_{1,\mathrm{ill}}(r,z) + \boldsymbol{E}_{2,\mathrm{ill}}(-r,-z)\right|^2, \tag{2}$$

$$\mathrm{PSF}_{\mathrm{det}}(\varepsilon r,\varepsilon z) = \left|\boldsymbol{E}_{1,\mathrm{det}}(\varepsilon r,\varepsilon z) + \boldsymbol{E}_{2,\mathrm{det}}(-\varepsilon r,-\varepsilon z)\right|^2, \tag{3}$$

where $\boldsymbol{E}_{\mathrm{ill}}$ and $\boldsymbol{E}_{\mathrm{det}}$ denote the electric field vector near the focus in the illumination and detection paths, respectively. The ratio between the illumination wavelength and the detection wavelength is represented by the parameter $\varepsilon = \lambda_{\mathrm{ill}}/\lambda_{\mathrm{det}}$. The subscripts 1 and 2 refer to the right and left focusing objectives, respectively. Here, the confocal pinhole in the detection path is assumed to be infinitely small.

For the case of high-NA focusing, the vectorial nature of the focused electromagnetic field should be taken into account. Based on the vector diffraction theory[27,28], the electric field vector in the focal region of a single lens can be written by

$$E(r,\varphi_p,z) = iC\iint_{\Omega} A(\theta)\sin\theta\sqrt{\cos\theta}\,T(\theta,\varphi)\exp[i\Delta(\theta)] \times \exp\{ikn[z\cos\theta + r\sin\theta\cos(\varphi-\varphi_p)]\}\mathrm{d}\theta\mathrm{d}\varphi, \tag{4}$$

where $E(r,\varphi_p,z)$ is the electric field vector at given point P. The azimuth angle of point P is denoted by φ_p. θ represents the polar angle. The origin of the cylindrical coordinates (r, φ_p, z) is the geometrical focus. C is the normalized constant, and $A(\theta)$ is the amplitude function of the incident beam at the pupil plane. $T(\theta,\varphi)$ is a 3×1 matrix related to the polarization of the incident beam. $\Delta(\theta)$ is the phase delay introduced by a phase plate. n is the refractive index of the imaging space, and k is the wave vector of the illumination wavelength.

When illuminated by higher-order RP-LG beams, the relative amplitude functions $A(\theta)$ and $T(\theta,\varphi)$ can be expressed as[11]

$$A(\theta) = \frac{\beta_0^2\sin\theta}{\sin^2\alpha}\exp\left(-\frac{\beta_0^2\sin^2\theta}{\sin^2\alpha}\right)L_p^1\left(\frac{2\beta_0^2\sin^2\theta}{\sin^2\alpha}\right), \tag{5}$$

$$T(\theta,\varphi) = \begin{bmatrix}\cos\theta\sin\varphi\\ \cos\theta\cos\varphi\\ \sin\theta\end{bmatrix}, \tag{6}$$

where α is the maximum aperture angle determined by the NA of the focusing objective. β_0 is the size parameter of higher-order LG RP beams, which is defined as the ratio of the pupil radius to the beam waist. L_p^1 is the generalized Laguerre polynomial with the radial mode number p.

For the case of circularly polarized beams, the beam shape is fundamental Gaussian. Consequently, $A(\theta)$ and $T(\theta,\varphi)$ can be expressed as

$$A(\theta)=\exp\left(-\frac{\beta_0^2\sin^2\theta}{\sin^2\alpha}\right), \tag{7}$$

$$T(\theta,\varphi)=\frac{1}{\sqrt{2}}\begin{bmatrix}1+(\cos\theta-1)(\cos^2\varphi+i\cos\varphi\sin\varphi)\\ i+(\cos\theta-1)(i\sin^2\varphi+\cos\varphi\sin\varphi)\\ \sin\theta(\cos\varphi+i\sin\varphi)\end{bmatrix}. \tag{8}$$

For a circular π phase plate, the phase delay introduced by this phase plate can be described as

$$\Delta(\theta)=\begin{cases}0(\alpha\le\theta)\\ \pi(0\le\theta\le\alpha)\end{cases}. \tag{9}$$

In subtraction imaging, the subtracted image is achieved by subtraction between two images obtained by different PSFs[23]. For the combination of a solid-shaped PSF and a doughnut-shaped PSF, the subtracted image can be expressed as[29]

$$\begin{aligned}I(x,y)&=I_{\text{bright}}(x,y)\text{-}\gamma I_{\text{dark}}(x,y)\\ &\propto \text{PSF}_{\text{sub}}(x,y)\otimes \text{Ob}(x,y),\end{aligned} \tag{10}$$

where $I_{\text{bright}}(x,y)$ and $I_{\text{dark}}(x,y)$ are images obtained by a solid-shaped $\text{PSF}_{\text{bright}}$ and a doughnut-shaped PSF_{dark}, respectively. γ is the subtraction coefficient, $\text{Ob}(x,y)$ is the fluorescence distribution emitted from a sample, and $\otimes$ is the convolution operator. The subtracted PSF of the imaging system is given by

$$\text{PSF}_{\text{sub}}=\text{PSF}_{\text{bright}}-\gamma\cdot\text{PSF}_{\text{dark}}. \tag{11}$$

For 4pi microscopy, the bright spot $\text{PSF}_{\text{bright}}$ and dark spot PSF_{dark} are the product of the illumination PSF_{ill} and the detection PSF_{det} under different illuminations. The larger the subtraction coefficient, the higher the resolution. However, excess subtraction will give rise to negative sidelobes in the subtracted PSF and unwanted artifacts will occur in the subtraction image[23]. Therefore, the value of the subtraction coefficient should be carefully chosen in order to avoid the occurrence of stronger negative sidelobes.

In the frequency domain, an optical imaging system can be considered as a low-pass filter and evaluated by OTF. Usually, the fine structure of samples is reflected by the high frequency. The OTF of the imaging system can be obtained by calculating the Fourier transform of the corresponding PSF and expressed as[30]

$$\begin{aligned}\text{OTF}(f_x,f_y,f_z)=&\iiint \text{PSF}(x,y,z)\\ &\times\exp[-2\pi i(xf_x+yf_y+zf_z)]\text{d}x\text{d}y\text{d}z.\end{aligned} \tag{12}$$

In the following simulations, the illumination wavelength is 350 nm, and the ratio of the excitation wavelength and the fluorescence wavelength is assumed to be 0.8. The size parameter β_0 and the NA of the focusing objective should be selected properly because those parameters can greatly affect the intensity distribution of the focal electric field[11]. Here, higher-order RP-LG beams are tightly focused by an oil-immersion objective with NA = 1.4. The refractive index of the immersion oil is 1.52, and the value of β_0 is 2.3. When the type-C 4pi imaging system is coherently illuminated by two counter-propagating RP-$\text{LG}_{1,1}$ beams, a solid-shaped PSF with a bright spot in the central region is produced.

Figure 2 gives the calculated lateral and axial PSF profiles of the 4pi imaging system for the cases of RP-$\text{LG}_{1,1}$ beam, RP beam (RP-$\text{LG}_{0,1}$), x-direction linearly polarized beam, and circularly polarized beam, respectively. According to the results in Fig. 2(a), it is obvious that the RP-$\text{LG}_{1,1}$ beam has the smallest full width at half-maximum (FWHM) in the transverse direction and then the highest lateral resolution. However, as shown in Fig. 2(b), the lateral resolution is enhanced at the cost of the largest extension in the axial direction accompanied by the strongest secondary axial sidelobes for the case of the RP-$\text{LG}_{1,1}$ beam, which is identical to the results of previous researches[11,14]. The relative height of the axial sidelobes generated by the RP-$\text{LG}_{1,1}$ beam is about 37% of the main peak. The poorer axial resolution and stronger sidelobes will decrease the sectioning ability and imaging quality of the 4pi system.

Figure 3(a) gives the normalized intensity distributions in the xz plane for the case of the RP-$\text{LG}_{1,1}$ beam. There is a bright spot in the central lobe, and a solid-shaped axial $\text{PSF}_{\text{bright}}$ with strong secondary sidelobes along the propagation direction is generated. It has been demonstrated that when a circular π phase plate is inserted in the

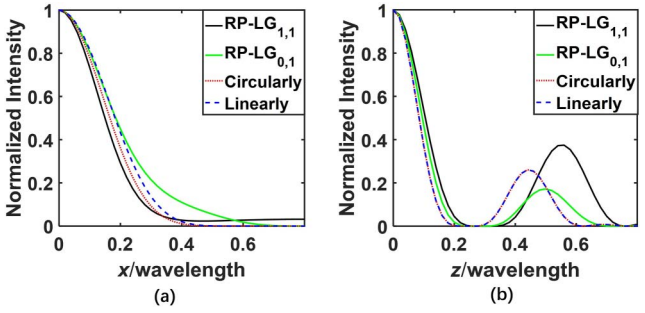

Fig. 2. Calculated PSF profiles (a) in the transverse direction and (b) in the axial direction for the RP-$\text{LG}_{1,1}$ beam, RP beam, circularly polarized beam, and x-axis linearly polarized beam, respectively. The peak intensities have been normalized to one.

illumination path, the power is shifted along the longitudinal direction, and intensity peaks at $z \neq 0$ can be observed[31]. Similarly, a doughnut-shaped focal spot in the longitudinal plane could be generated by inserting a circular π phase plate in one arm of the 4pi focusing system[32]. Compared with linear and elliptical polarizations, a uniform intensity distribution in the xy plane is achievable for circular polarization. Here, the combination of two counter-propagating circularly polarized beams and a circular π phase plate inserted in one arm of the illumination path is used to generate a doughnut-shaped axial PSF. As shown in Fig. 3(b), under circularly polarized illumination, a doughnut-shaped axial $\mathrm{PSF_{dark}}$ with a dark spot in the z axis is formed. There are many sidelobes, and the strongest sidelobes are comparable to the central dark spot. Figure 3(c) presents the axial profiles of the doughnut-shaped $\mathrm{PSF_{dark}}$ for different values of NA when $\beta_0 = 1.0$. The relative magnitude of the sidelobes is enhanced with decreasing NA. In addition, the locations of the sidelobes can be shifted along the axial direction by adjusting the value of NA. For NA = 1.3, Fig. 3(d) shows the axial profiles of the $\mathrm{PSF_{dark}}$ for different values of β_0. Obviously, the size parameter can also affect the relative magnitude and location of the sidelobe. For those aforementioned reasons, when illuminated by circularly polarized beams, the effective NA of the focusing objective is deliberately reduced to be 1.3 by tuning the diaphragms in the optical path, and the value of β_0 is 1.0. Consequently, the strongest sidelobes of the $\mathrm{PSF_{dark}}$ match very well with the secondary sidelobes of the $\mathrm{PSF_{bright}}$, as illustrated by the red dashed and green dotted lines in Fig. 3(e), respectively. When the value of the subtraction coefficient γ is 0.3, the effective $\mathrm{PSF_{sub}}$ of subtractive imaging is calculated by using Eq. (11). The blue solid line in Fig. 3(e) shows the axial profile of the $\mathrm{PSF_{sub}}$ in the z axis. The FWHM of the $\mathrm{PSF_{sub}}$ is decreased from 0.21λ to 0.15λ, and the axial sidelobes are significantly reduced from 37% to about 10% of the central lobe. There are negative intensities in the sidelobes. But, those negative intensities are not very strong, and the effect on the imaging quality can be tolerable. The relative strength of the sidelobes is very important for subtraction imaging. If the central dark spot of the $\mathrm{PSF_{dark}}$ is much stronger than the strongest sidelobes, sidelobe suppression is spoiled by unwanted artifacts in the subtraction image induced by stronger negative intensities. For simplicity, those results are not shown in this Letter. The two-dimensional (2D) intensity distribution of the subtracted axial $\mathrm{PSF_{sub}}$ in the xz plane is given by Fig. 3(f). Obviously, the sidelobes are greatly suppressed by subtraction of the $\mathrm{PSF_{dark}}$ from the $\mathrm{PSF_{bright}}$, and a much narrower central bright spot remains in the $\mathrm{PSF_{sub}}$.

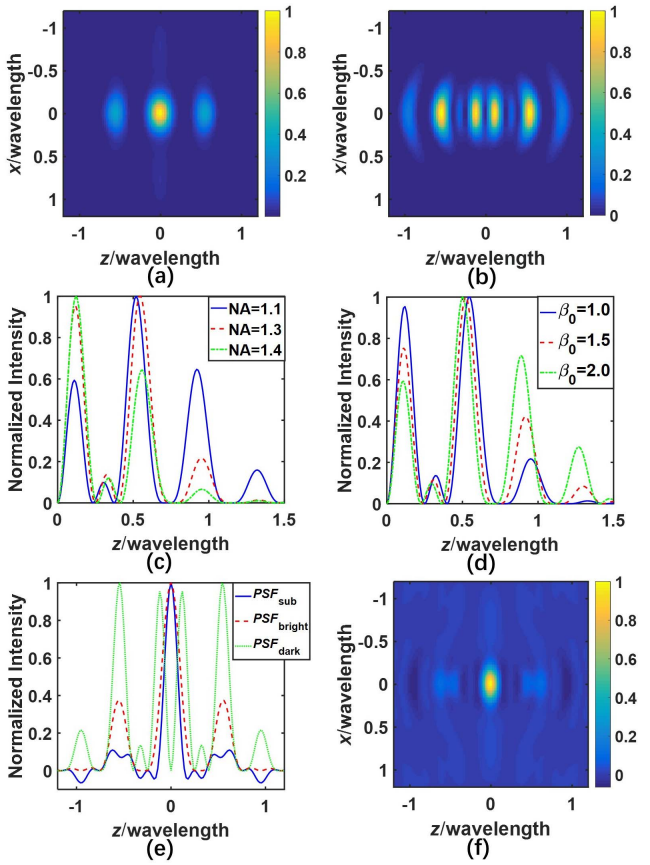

Fig. 3. 2D intensity distributions of the (a) $\mathrm{PSF_{bright}}$ and (b) $\mathrm{PSF_{dark}}$ in the xz plane ($y = 0$). Axial profiles of the $\mathrm{PSF_{dark}}$ for different values of (c) NA and (d) β_0, respectively. (e) Axial profiles of the $\mathrm{PSF_{bright}}$ (red dashed line), $\mathrm{PSF_{dark}}$ (green dotted line), and $\mathrm{PSF_{sub}}$ (blue solid line) in the z axis. (f) Intensity distribution of the $\mathrm{PSF_{sub}}$ in the xz plane ($y = 0$).

Figure 4 gives the normalized axial OTF profiles calculated by performing the Fourier transform of the corresponding $\mathrm{PSF_{bright}}$ and $\mathrm{PSF_{sub}}$, respectively. The OTF for the case of the RP-$\mathrm{LG_{1,1}}$ beam presents an irregular profile, which is similar to the result for linearly polarized illumination in Ref. [21] and attributed to axial sidelobes. Although, after subtraction, the cut-off frequency is almost unchanged, the relative magnitude of high frequencies of the $\mathrm{OTF_{sub}}$ is greatly improved, and the axial gaps are partially filled, especially for the range from 1.2 NA/λ to 3.3 NA/λ, which indicates that the fine structure of the samples is enhanced, and the axial resolution is increased.

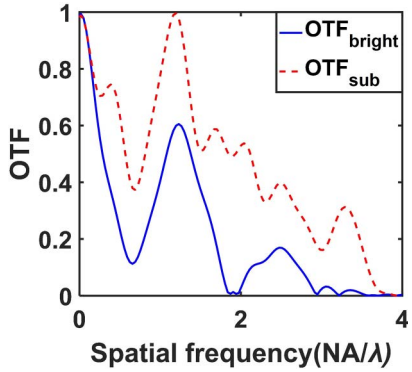

Fig. 4. Corresponding axial OTFs calculated for the $\mathrm{PSF_{bright}}$ (blue solid line) and $\mathrm{PSF_{sub}}$ (red dashed line) when the value of γ is 0.3.

The lateral intensity distributions of different PSFs in the xy plane ($z = 0$) are illustrated by Figs. 5(a), 5(b), and 5(c), respectively. As shown in Figs. 5(a) and 5(b), there is a solid-shaped spot for the case of the RP-$LG_{1,1}$ beam, whereas a doughnut-shaped spot is presented under circularly polarized illumination. It should be noted that the relative strength of the doughnut-shaped spot in the focal plane is much weaker than that of the solid-shaped spot. After subtraction, the size of the bright central spot is nearly unchanged, as shown in Fig. 5(c). Figure 5(d) gives the lateral profile of the subtracted intensity distribution along the x axis when $\gamma = 0.3$. For comparison, the corresponding profiles of the solid-shaped spot and doughnut-shaped spot are also shown. The green dotted line denotes the intensity profile of the PSF_{dark} itself before being multiplied by the subtraction coefficient. In subtractive imaging, the contribution of the PSF_{dark} is further weakened. Therefore, the lateral FWHM of the subtracted PSF remains unchanged and is 0.3λ. Figure 5(a) also shows that there is the lateral sidelobe in the transverse intensity distribution of the PSF_{bright}. However, as shown in Fig. 5(d), this lateral sidelobe is just about 3% of the central lobe and nearly has no influence on the image quality.

Finally, a 3D sample with a 3-by-3-by-3 point array [as shown in Fig. 6(a)] is designed to verify the performance of subtractive imaging in 4pi microscopy. According to Fig. 6(b), the distance between two adjacent points of the sample is 0.3λ in the lateral direction and equivalent to the transverse FWHM of the bright spot PSF_{bright}. However, the distance along the axial direction is deliberately chosen to be 0.175λ and a bit smaller than the axial FWHM of the PSF_{bright}.

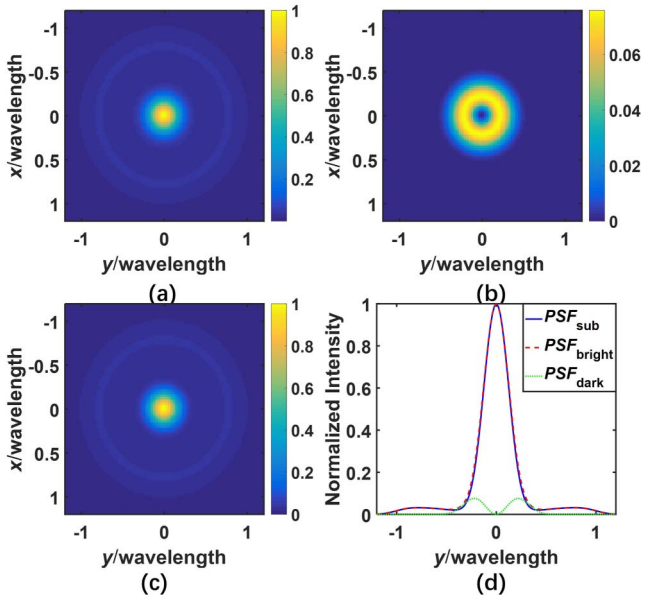

Fig. 5. Transverse intensity distributions in the focal plane when illuminated by (a) RP-$LG_{1,1}$ beams and (b) circularly polarized beams, respectively. (c) Intensity distributions of the PSF_{sub} in the xy plane ($z = 0$). (d) The corresponding lateral profiles of intensity distributions along the x axis.

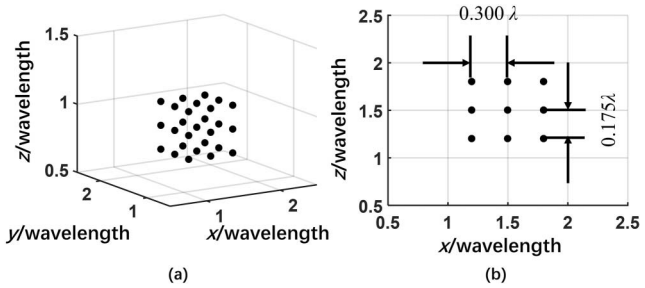

Fig. 6. (a) 3D point array sample. (b) Cross section of the 3D sample in the xz plane.

Figure 7(a) gives image reconstruction generated by the convolution of the 3D sample with the bright spot PSF_{bright} for the cases of the RP-$LG_{1,1}$ beam. The corresponding xz slice and xy slice are illustrated by Figs. 7(b) and 7(c), respectively. The nine points in the xy plane can be just resolved. However, because the axial resolution is not high enough in comparison to the axial distance between two adjacent points, the image in the xz plane exhibits three layers along the x direction, and the fine structure of the sample along the z axis is completely blurred by the artifacts induced by the strong axial sidelobes. Figures 7(d), 7(e), and 7(f) show the results of subtractive imaging by the convolution of the 3D sample with the subtracted PSF_{sub}. According to Fig. 7(e), the points in the xz plane can be clearly distinguished, which

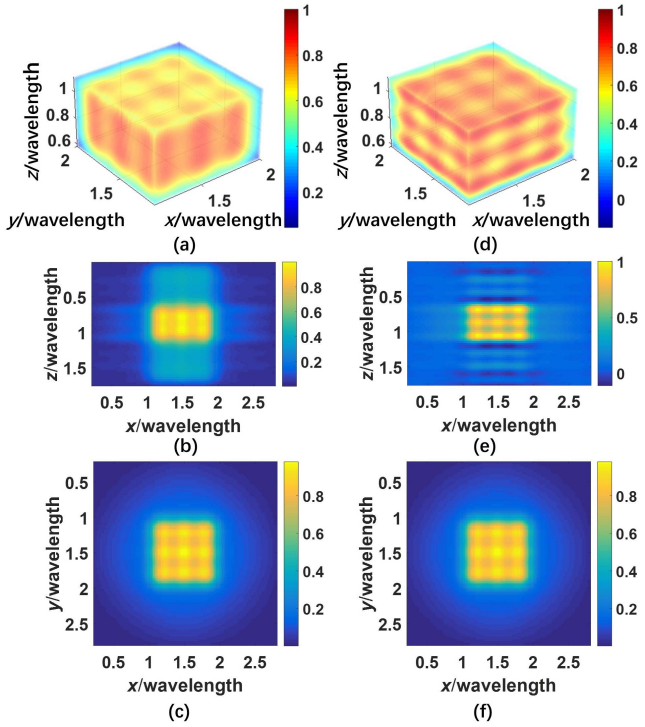

Fig. 7. (a) 3D image reconstruction of the point array sample with the PSF_{bright}. (b) xz slice and (c) xy slice of the image in (a). (d) 3D image reconstruction of the point array sample with the PSF_{sub}. (e) xz slice and (f) xy slice of the subtracted image in (d).

indicates the enhancement of the axial resolution in 4pi microscopy by subtractive imaging.

In summary, it has been demonstrated that a combination of a first-order LG-RP beam and a modulated circularly polarized beam is suitable for subtractive imaging of 4pi microscopy. A bright spot PSF_{bright} with strong axial sidelobes is produced by tight focusing RP-$LG_{1,1}$ beams, whereas, under circularly polarized illumination, a doughnut-shaped PSF_{dark} with a dark spot along the optical axis is formed when one arm of the illumination path is modulated by a circular π phase plate. The sidelobes of the subtracted PSF_{sub} have been greatly suppressed, and the axial resolution is effectively enhanced. The image subtraction does not compromise the lateral resolution. The 3D sample is imaged twice by scanning with the solid-shaped PSF and doughnut-shaped PSF, respectively. By subtracting the images obtained with those two different PSFs, the image quality is much higher as a result of the significant suppression of sidelobes and the increase of the axial resolution. Our investigations can provide a new method to optimize 4pi microscopy with a higher-order LG-RP beam and are beneficial for the development of high-resolution 3D microscopy.

This work was supported by the Key Program of the Natural Science Foundation of Tianjin (No. 19JCZDJC32700) and the Science and Technology Support Program of Tianjin (No. 17YFZCSY00740). This work was partially carried out at the Engineering Research Center of Thin Film Photo-electronics Technology, Ministry of Education.

References

1. W. Volker and S. W. Hell, Phys. Rev. Lett. **94**, 143903 (2005).
2. S. W. Hell, Nat. Methods **6**, 24 (2009).
3. S. Quabis, R. Dorn, M. Eberler, O. Glöckl, and G. Leuchs, Opt. Commun. **179**, 1 (2000).
4. R. Dorn, S. Quabis, and G. Leuchs, Phys. Rev. Lett. **91**, 233901 (2003).
5. Q. Zhan, Opt. Express **12**, 3377 (2004).
6. L. Novotny, M. R. Beversluis, K. S. Youngworth, and T. G. Brown, Phys. Rev. Lett. **86**, 5251 (2001).
7. M. Matthias, V. Romano, and T. Feurer, Appl. Phys. A **86**, 329 (2007).
8. Y. Kozawa and S. Shunichi, J. Opt. Soc. Am. A **27**, 399 (2010).
9. M. Yoshida, Y. Kozawa, and S. Sato, Opt. Lett. **44**, 883 (2019).
10. Y. Kozawa and S. Sato, J. Opt. Soc. Am. A **29**, 2439 (2012).
11. Y. Kozawa and S. Sato, J. Opt. Soc. Am. A **24**, 1793 (2007).
12. Y. Kozawa, T. Hibi, A. Sato, H. Horanai, M. Kurihara, N. Hashimoto, H. Yokoyama, T. Nemoto, and S. Sato, Opt. Express **19**, 15947 (2011).
13. Y. Kozawa and S. Sato, Opt. Express **23**, 2076 (2015).
14. G. Chen, F. Song, and H. Wang, Opt. Lett. **38**, 3937 (2013).
15. S. Hell and E. H. K. Stelzer, J. Opt. Soc. Am. A **9**, 2159 (1992).
16. M. Nagorni and S. W. Hell, J. Opt. Soc. Am. A **18**, 36 (2001).
17. S. Hell and E. H. K. Stelzer, Opt. Commun. **93**, 277 (1992).
18. S. Hell, W. S. Lindek, and E. H. K. Stelzer, J. Mod. Opt. **41**, 675 (1994).
19. M. Schrader, S. W. Hell, and H. T. M. van der Voort, J. Appl. Phys. **84**, 4033 (1998).
20. M. Martınez-Corral, A. Pons, and M. T. Caballero, J. Opt. Soc. Am. A **19**, 1532 (2002).
21. M. Martınez-Corral, M. T. Caballero, A. Pons, and P. Andrés, Micron **34**, 319 (2003).
22. S. J. Hewlett and T. Wilson, Mach. Vis. Appl. **4**, 233 (1991).
23. S. Segawa, Y. Kozawa, and S. Sato, Opt. Lett. **39**, 3118 (2014).
24. Y. Zhang, L. Kong, H. Xie, X. Han, and Q. Dai, Opt. Express **26**, 21518 (2018).
25. S. Deng, Y. Xiao, J. Hu, J. Chen, Y. Wang, and M. Liu, Chin. Opt. Lett. **16**, 111801 (2018).
26. H. Jia, X. Yu, Y. Yang, X. Zhou, S. Yan, C. Liu, M. Lei, and B. Yao, J. Biophoton. **12**, e201800094 (2019).
27. B. Richards and E. Wolf, Proc. R. Soc. Lond. A Math. Phys. Sci. **253**, 358 (1959).
28. K. S. Youngworth and T. G. Brown, Opt. Express **7**, 77 (2000).
29. G. Zhao, C. Kuang, Z. Ding, and X. Liu, Opt. Express **24**, 23596 (2016).
30. S. Kimura and C. Munakata, J. Opt. Soc. Am. A **6**, 1015 (1989).
31. X. Hao, C. Kuang, T. Wang, and X. Liu, J. Opt. **12**, 115707 (2010).
32. S. Liu, S. You, Y. Fang, Y. Wang, C. Kuang, and X. Liu, J. Mod. Opt. **63**, 1145 (2016).